Comp. Part. Mech.
DOI 10.1007/s40571-017-0173-4

A hybrid Lagrangian Voronoi–SPH scheme

D. Fernandez-Gutierrez[1] · **A. Souto-Iglesias**[2] · **T. I. Zohdi**[1]

Received: 28 June 2017 / Revised: 27 September 2017 / Accepted: 21 October 2017

Abstract A hybrid Lagrangian Voronoi–SPH scheme, with an explicit weakly compressible formulation for both the Voronoi and SPH sub-domains, has been developed. The SPH discretization is substituted by Voronoi elements close to solid boundaries, where SPH consistency and boundary conditions implementation become problematic. A buffer zone to couple the dynamics of both sub-domains is used. This zone is formed by a set of particles where fields are interpolated taking into account SPH particles and Voronoi elements. A particle may move in or out of the buffer zone depending on its proximity to a solid boundary. The accuracy of the coupled scheme is discussed by means of a set of well-known verification benchmarks.

Keywords CFD · SPH · Voronoi · Coupling

1 Introduction

The smoothed particle hydrodynamics (SPH) method is known for its flexibility to easily model complex physics [20] and its outstanding conservation properties, but also due to its limitations in discretization adaptivity, accuracy and implementation of boundary conditions, among others. Apart from performing modifications in the scheme to overcome these limitations, which in any case penalize their conservation properties, an alternative approach is to couple the scheme with other methods, splitting the physical domain in disjunct regions where either the SPH method or the coupled one is applied.

Very recent examples have explored the coupling of SPH and mesh-based finite volume method solvers [13,18,22] with promising results. An additional appealing approach is to couple SPH with another meshless method with some improved characteristics. The fully Lagrangian version of Voronoi particle hydrodynamics (VPH) [12] emerges as an attractive option for this kind of coupling.

The fully Lagrangian VPH has been developed from the Voronoi dynamics method created by Serrano et al. [25,26], who developed a meshless scheme that is first-order consistent for the first-order differential operators, regardless of the geometrical distribution of the particles. The method was conceived for molecular dynamics simulations, and entropy evolution equation was part of the formalism.

The idea of a hybrid Lagrangian Voronoi–SPH scheme was first proposed by Barcarolo et al. [4,5]. They used a finite volume formulation for the Voronoi sub-domain and Riemann-SPH for the SPH sub-domain. The coupling was achieved by considering the SPH particles as Voronoi ones when interacting with Voronoi particles, and vice versa. This coupling does not preserve the order of both methods when taken to the particle level, and some improvements are required.

The present paper proposes a method in which VPH is used for the Voronoi region and δ-SPH is used for the SPH zone. A buffer zone to couple the dynamics of both sub-domains is developed. This zone is formed by a set of particles whose derivatives take into account both SPH and Voronoi formulations. VPH is used for those regions close

✉ D. Fernandez-Gutierrez
dfg82@berkeley.edu

A. Souto-Iglesias
antonio.souto@upm.es

T. I. Zohdi
zohdi@berkeley.edu

[1] Department of Mechanical Engineering, University of California at Berkeley, Berkeley, CA, USA

[2] CEHINAV, DMFPA, ETSIN, Universidad Politécnica de Madrid, 28040 Madrid, Spain

Published online: 06 November 2017

to the solid boundaries, in order to accurately implement the solid boundary conditions.

The long-term applications that motivate present research, such as 3D printing, are mostly referred to liquids. They can, in practical terms, be accurately modeled as weakly compressible barotropic fluids. This way, by neglecting entropy influence, the pressure becomes a function only of density in an equation of state. Under this assumption, the energy equation becomes uncoupled, leading to the formalism and structure of the method being similar to SPH, thus facilitating their coupling.

In the formulation developed herein, a Voronoi graph is computed in every time step from the particle positions. The resulting Voronoi cells allow us to associate to each particle a certain volume, and considering their mass, a derived density.

The paper presents first the continuous model and the coupled schemes. The coupling strategy is then discussed. How boundary conditions are implemented deserves a dedicated analysis that follows next. The accuracy and conservation properties of the scheme are discussed thereafter. The method is then challenged with some verification cases and validation benchmarks. Conclusions and future lines of work are enumerated to close the paper.

2 Governing equations

The scope of this research covers monophasic free-surface incompressible viscous flow. In order to model incompressibility, the fluid is assumed to be barotropic and weakly compressible. This second hypothesis is generally used within the SPH method in order to avoid the solution of a Poisson equation for the pressure field, and in order to use an explicit time integration for the discrete equations. Under these hypotheses, the Navier–Stokes equations read:

$$\begin{cases} \dfrac{\mathrm{d}\rho}{\mathrm{d}t} + \rho\,\nabla\cdot\boldsymbol{u} = 0, \\ \rho\,\dfrac{\mathrm{d}\boldsymbol{u}}{\mathrm{d}t} = \rho\,\boldsymbol{g} - \nabla p + \nabla\cdot(2\mu\,\mathbb{D}) + \nabla\left(\lambda\,(\nabla\cdot\boldsymbol{u})\right), \\ \dfrac{\mathrm{d}\boldsymbol{r}}{\mathrm{d}t} = \boldsymbol{u}, \qquad p = c_0^2\,(\rho-\rho_0), \end{cases} \tag{1}$$

where $\mathrm{d}/\mathrm{d}t$ is the Lagrangian derivative, p the pressure, c_0 the constant sound velocity, ρ the fluid density, and ρ_0 the reference density. The flow velocity, $\boldsymbol{u}$, is defined as the material derivative of a fluid material point at the position $\boldsymbol{r}$. $\mathbb{D}$ is the rate of deformation tensor, $\mathbb{D} = (\nabla\boldsymbol{u} + \nabla\boldsymbol{u}^{\mathrm{T}})/2$.

In the weakly compressible regime, the compressible viscosity term is negligible for the flows studied in this work (see, e.g., [17] and [9]) and it is not further considered. Under these conditions, and with the additional hypothesis of constant dynamic viscosity, the momentum equation becomes:

$$\rho\,\frac{\mathrm{d}\boldsymbol{u}}{\mathrm{d}t} = \rho\,\boldsymbol{g} - \nabla p + \mu\,\nabla^2\boldsymbol{u}. \tag{2}$$

Boundary conditions will be discussed specifically when discussing the numerical methods.

3 Method

3.1 δ-SPH scheme

For the SPH sub-domain, the δ-SPH scheme proposed by Antuono et al. [1,2] is adopted to compute the numerical solution. The evolution equations of a generic i-th fluid particle read:

$$\begin{cases} \dfrac{\mathrm{d}\rho_a}{\mathrm{d}t} = -\rho_a \displaystyle\sum_b (\boldsymbol{u}_b - \boldsymbol{u}_a)\cdot\nabla_a W_{ab}\,V_b \\ \qquad\qquad + \delta\,\overline{h}_{ab}\,c_0\,\sum_b \psi_{ab}\,\frac{(\boldsymbol{r}_b-\boldsymbol{r}_a)\cdot\nabla_a W_{ab}}{\|\boldsymbol{r}_b-\boldsymbol{r}_a\|^2}\,V_b \\ \dfrac{\mathrm{d}\boldsymbol{u}_a}{\mathrm{d}t} = \boldsymbol{g}_a - \dfrac{1}{\rho_a}\displaystyle\sum_b (p_b + p_a)\,\nabla_a W_{ab}\,V_b \\ \qquad\qquad + \nu\,\frac{\rho_0}{\rho_a}\,\sum_b \pi_{ab}\,\nabla_a W_{ab}\,V_b \\ \dfrac{\mathrm{d}\boldsymbol{r}_a}{\mathrm{d}t} = \boldsymbol{u}_a, \quad p_a = c_0^2\,(\rho_a-\rho_0) + p_0, \quad \left(\dfrac{h_a}{h_0}\right)^d = \dfrac{\rho_0}{\rho_a}, \end{cases} \tag{3}$$

where ρ_a, p_a, $\boldsymbol{u}_a$ and V_a are, respectively, the density, the pressure, the velocity and the volume of the a-th particle, ρ_0 the reference density, p_0 a background pressure, and ψ_{ab} is Cercos-Pita et al's [7] artificial diffusive term. The symbol ∇_a indicates the differentiation with respect to the position of the a-th particle while $\boldsymbol{g}_a$ denotes the body force acting on it. Finally, W_{ab} is the kernel function. In this work, a C2 Wendland kernel with compact support of radius $2h_a$, where h_a is the *smoothing length*, has been used. The smoothing length may vary slightly from the reference value h_0 along the simulation for each particle so that the number of neighbors remains approximately constant. The sound speed, c_0, is set in order to guarantee density variations smaller than $0.01\rho_0$, and $\overline{h}_{ab}$ is defined as the average smoothing length of particles a and b. The (dimensionless) parameter δ is set to 0.1 in all the simulations. In the present work, $h_0/\Delta x = 2$, that corresponds to an average number of particles in the kernel support of about 50.

3.2 Voronoi particle hydrodynamics (VPH)

3.2.1 General

In the Voronoi tessellation, a polyhedral volume, which encompasses the space closer to every particle than to any other, is assigned to that particle. Based on this partition of the fluid domain, the governing Eq. (1) can be discretized.

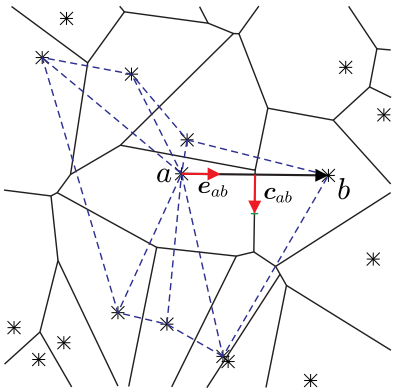

Fig. 1 Section of a Voronoi diagram for a set of particles marked with asterisks. All the triangles in the dual Delaunay tessellation with vertex in a are drawn with dashed lines. The vectors $\boldsymbol{e}_{ab}$ and $\boldsymbol{c}_{ab}$ needed to calculate the derivative of the volume are also marked

The Voronoi scheme used in this paper has as a precursor the one of Hess and Springel [12].

In this model, it is assumed that each particle conserves mass. For this reason, the density of a generic particle a can simply be estimated as:

$$\rho_a = \frac{m_a}{V_a}, \tag{4}$$

where m_a and V_a are, respectively, the mass and volume assigned to particle a.

Since density evolves with this rule, the continuity equation in (1) is not integrated in time. Regarding the pressure gradient in the momentum equation, the gradient estimate of Serrano and Español [26] is used:

$$(\nabla p)_a \approx \frac{1}{V_a} \sum_{b \neq a} A_{ab} \left[(p_a + p_b) \frac{\boldsymbol{e}_{ab}}{2} + (p_b - p_a) \frac{\boldsymbol{c}_{ab}}{r_{ab}} \right], \tag{5}$$

where $\boldsymbol{e}_{ab}$ is the unit vector from particles a to b, with positions $\boldsymbol{r}_a, \boldsymbol{r}_b$ (see Fig. 1):

$$\boldsymbol{e}_{ab} := \frac{\boldsymbol{r}_b - \boldsymbol{r}_a}{|\boldsymbol{r}_b - \boldsymbol{r}_a|}. \tag{6}$$

It is stressed here that the notation $\boldsymbol{e}_{ab}$, with the vector pointing from a to b, is used in order to keep Hess and Springel's [12]'s notation. However, in the SPH formulation, when a vector subindex is ab, it implies it is obtained by subtracting the value in particle a from that in particle b.

In formula (5), A_{ab} is the area, in the Voronoi diagram, of the face between particles a and b. The vector $\boldsymbol{c}_{ab}$ is defined as going from the midpoint between a and b to the centroid of the face between such particles.

Serrano and Español [26] demonstrated that the gradient formula (5) is first-order accuracy independently of the distribution of the particles.

With regard to the viscous term, it has been formulated [see Eq. (2)] as the Laplacian of the velocity field. In order to discretize it, the Laplacian of each component of the velocity field will be treated independently, something valid for Cartesian coordinates. This way, and following Hess and Springel's [12] estimate for the Laplacian of a scalar field,

$$\begin{aligned} \left(\nabla^2 u^i\right)_a &\approx \frac{1}{V_a} \int_{V_a} \nabla^2 u^i \, \mathrm{d}V \\ &= \frac{1}{V_a} \sum_{b \neq a} \int_{A_{ab}} \nabla u^i \cdot \mathbf{d}\boldsymbol{A}, \end{aligned} \tag{7}$$

where the divergence theorem has been used.

The dot product inside the integral is the directional derivative of the i-th component of the velocity across the normal of each of the faces of the element a. This directional derivative can be approximated in first order as $(u_b^i - u_a^i)/r_{ab}$, leading to the following estimate for the velocity Laplacian:

$$\left(\nabla^2 \boldsymbol{u}\right)_a \approx -\frac{1}{V_a} \sum_{b \neq a} \frac{\boldsymbol{u}_{ab}}{r_{ab}} A_{ab}, \tag{8}$$

where the vector notation for the Laplacian is recovered. The order of this formula is not clearly established in the literature. Serrano [25] used it to simulate a shear stationary flow, showing that the schemes display extra dissipation when particles are in disordered configurations while it renders accurate results for orderly ones. For an extensive discussion on the properties of the Laplacian operator in Voronoi and Delaunay tessellations, the reader is referred to Duque et al. [10] and references therein.

3.3 Coupling

A hybrid Voronoi–SPH scheme has been developed. A fully Lagrangian formulation for the Voronoi and SPH subdomains is considered. A buffer zone to couple the dynamics of both sub-domains is used. This zone is formed by a set of particles whose fields take into account both SPH particles and Voronoi elements. A particle may move in or out of the buffer zone depending on its proximity to a solid boundary.

How the purely SPH, Voronoi and buffer zones are defined is shown in the sketch present in Fig. 2. The Voronoi zone is defined adjacent to the solid boundaries. Its width is such that particles outside the Voronoi zone will be at distance larger than $2\,h_{\max}$, with $h_{\max}$ being the largest h, of the closest solid boundary, so that no SPH particle will have any interaction with the solid boundaries.

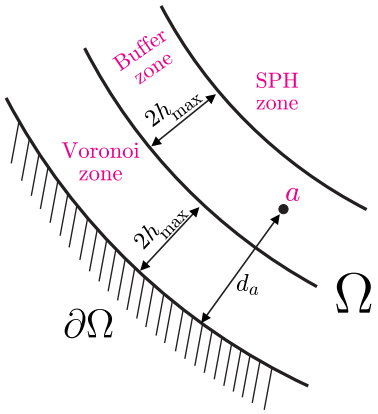

Fig. 2 Sketch with definition of Voronoi, SPH and buffer zones

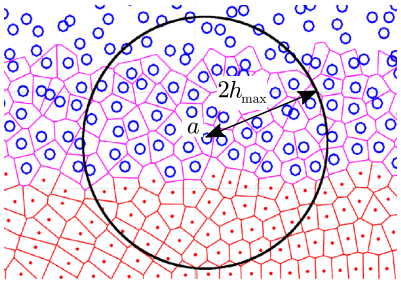

Fig. 3 Example of particle in the buffer zone. Voronoi (with tessellation diagram), buffer and SPH zones are shown in the figure

Regarding the buffer zone, a particle a is assumed to belong to the buffer zone if and only if it may simultaneously have Voronoi and SPH particles inside the SPH kernel support of radius $2\,h_{\max}$ with center at such particle. For instance, the particle a in Figs. 2 and 3 belongs to the buffer zone.

The SPH zone is defined as the rest of the fluid domain.

For the particles outside the buffer zone, the fields are interpolated with the scheme corresponding to the subdomain type. Therefore, the value of a certain field A at a particle a when it is in the buffer will be defined as:

$$A_a := \omega_a\, A_a^{\mathrm{SPH}} + (1-\omega_a)\, A_a^{\mathrm{Vor}}, \tag{9}$$

where A_a^{SPH} is the field value obtained through the SPH interpolation, A_a^{Vor} is the field value obtained with the Voronoi interpolation and ω is a weight defined so that the coupling is $\mathcal{C}^1$. We must stress that this condition is a first best guess, inspired by the h^2 order of the SPH interpolation studied in detailed by Quinlan et al. [24]. However, other alternatives are of course possible. To this aim, the value A_a should tend to A_a^{Vor} as the particle gets close to the Voronoi zone and should tend to A_a^{SPH} as the particle gets close to the SPH zone. A factor r is defined using the distance d_a between the particle a and the closest solid wall:

$$r_a := \frac{d_a - 2\,h_{\max}}{2\,h_{\max}}, \tag{10}$$

and ω_a is the output of a third-grade polynomial in r_a which allows to have the required $\mathcal{C}^1$ class for the coupling scheme (9):

$$\omega_a := r_a^2\,(3 - 2\,r_a). \tag{11}$$

However, density is computed directly from the Voronoi cell while in SPH is obtained integrating in time the continuity equation. It was observed that coupling directly both values led to rougher transitions due to the different nature of their origin. Therefore, the VPH scheme estimates the density rate of change in the buffer zone following Eq. (12), so the coupling is applied on the time derivatives and the resulting value is used to evolve the density in time.

$$\left.\frac{\mathrm{d}\rho}{\mathrm{d}t}\right|_a = -\rho_a(\nabla\cdot\boldsymbol{v})_a \approx \frac{\rho_a}{V_a}\sum_{b\neq a} A_{ab}(\boldsymbol{v}_a - \boldsymbol{v}_b)\cdot\left[\frac{\boldsymbol{e}_{ab}}{2} + \frac{\boldsymbol{c}_{ab}}{r_{ab}}\right]. \tag{12}$$

3.4 Boundary conditions (BCs)

3.4.1 Grid

The range of interaction of a particle is finite in both SPH and Voronoi schemes. For this reason, it is convenient to split the fluid domain in cells such that the interaction range of the particles belonging to one cell will be restricted to that cell plus the neighboring ones. To achieve this, the cells of that grid must have as length $2h_{\max}$ in the case of SPH and $2\max(r_{ab})$ for the Voronoi scheme. This way, in order to find neighboring particles, it will only be necessary to search them in your own cell and in the neighboring ones.

3.4.2 Solid boundaries

In present coupled scheme, interaction with solid boundaries only takes place for Voronoi particles, and therefore, solid BCs refer only to Voronoi particles. The solid boundary is discretized in present scheme as a polygonal line (see Fig.4). The main challenge for imposing BCs lies on achieving that the solid boundary becomes the actual boundary of well-defined Voronoi elements. Therefore, a prior step to imposing BCs on Voronoi cells is to construct and adequate Voronoi tessellation. For the time being, let us assume that there is a Voronoi tessellation that fulfills the referred conditions.

In order to show how BCs are imposed, a sample element adjacent to a boundary, and whose center is particle a, is displayed in Fig. 4. For each boundary segment in the element a (the same label is used for the element and its center), a

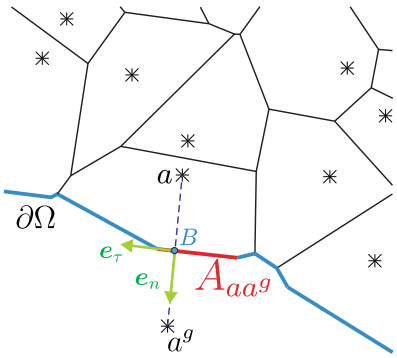

Fig. 4 Section of a Voronoi diagram close to a solid boundary

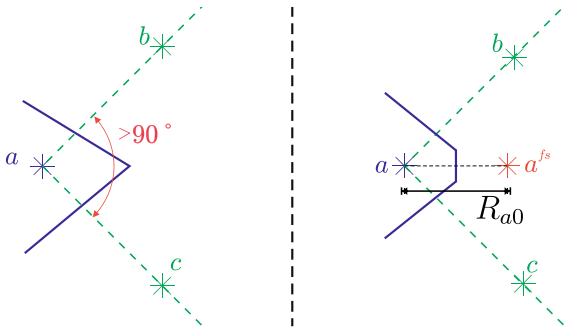

Fig. 5 Voronoi free-surface particle detection and edge definition

reflected point a^g of center a with respect to that segment is created. This point is necessary to guarantee that the domain boundary is covered by the edges of tessellation elements. Unlike ghost particles in SPH, these reflected points are used only to create the Voronoi tessellation, but do not play any role in the mathematical treatment of the flow fields. Once the solid boundaries become part of the perimeter of the Voronoi cells, the BCs can be enforced directly in the Voronoi differential operators (5, 8) by extrapolating the known physical properties at the boundaries to a^g:

1. No-slip BC: the flow velocity tends to the boundary velocity $\boldsymbol{u}_B$ as a fluid element gets close to the boundary. To achieve this:

$$\boldsymbol{u}_{a^g} = 2\,\boldsymbol{u}_B - \boldsymbol{u}_a. \tag{13}$$

2. Free slip BC: the normal velocity tends to the boundary normal velocity as a fluid element gets close to the boundary. To achieve this, Eq. (13) is projected on the exterior normal $\boldsymbol{e}_n$:

$$\boldsymbol{u}_{a^g} \cdot \boldsymbol{e}_n = (2\,\boldsymbol{u}_B - \boldsymbol{u}_a) \cdot \boldsymbol{e}_n, \tag{14}$$

while the tangential component remains unaltered:

$$\boldsymbol{u}_{a^g} \cdot \boldsymbol{e}_\tau = \boldsymbol{u}_a \cdot \boldsymbol{e}_\tau. \tag{15}$$

3. Following [16], the pressure field p_g is mirrored on the ghost particles to enforce the following Neumann condition at the boundary (resulting from projecting, on the boundary normal, the pressure gradient obtained from the momentum equation):

$$\frac{\partial p}{\partial \boldsymbol{e}_n} = \rho \left[\boldsymbol{g} \cdot \boldsymbol{e}_n - \frac{\mathrm{d}\boldsymbol{u}_B}{\mathrm{d}t} \cdot \boldsymbol{e}_n + \nu \nabla^2 \boldsymbol{u} \cdot \boldsymbol{e}_n \right], \tag{16}$$

with the last term being generally negligible. Pressure at the ghost particle is obtained by linear extrapolation:

$$p_a^g = p_a + \frac{\partial p}{\partial \boldsymbol{e}_n} \cdot (\boldsymbol{r}_a^g - \boldsymbol{r}_a). \tag{17}$$

3.4.3 Free surface

There is not special treatment for SPH regarding the free surface. The free-surface boundary conditions (kinematic and free-stress) are a direct consequence of the Lagrangian and explicit nature of the scheme.

For Voronoi elements, a specific treatment is proposed. In order to detect whether a Voronoi element a is bounded by a free surface, the angle between the lines connecting the center of element a with the center of neighbor elements is explored. If for any set of three particles (see left panel of Fig. 5), this angle is greater than 90° and any neighboring particle is already a free-surface one, then a is labeled as free-surface and treated as such. To this aim, a virtual particle a^{fs} is created at a distance l_{a0} in the bisector which has led to the free-surface detection (see right panel of Fig. 5). This virtual particle is then considered for the Voronoi tessellation. The distance l_{a0} is defined as follows:

$$l_{a0} = V_{a0}^{1/d}, \quad V_{a0} = m_a/\rho_0, \tag{18}$$

with d being the dimensionality of the problem.

Defining the particle this way induces the creation of an edge for element a in between a and a^{fs} after the subsequent tessellation (see right panel of Fig. 5), which leads to the volume of element a being close to V_{a0}. Since mass is conserved, the density of such element ρ_a will be close to ρ_0 and therefore the pressure at the free-surface elements will be zero. This approach approximately fulfills the free-surface dynamic boundary condition, with the kinematic one is implicitly satisfied by the Lagrangian nature of the scheme.

3.4.4 Voronoi free-surface particle close a solid boundary

When a free-surface SPH particle approaches a solid boundary it is treated as a Voronoi particle, consistently with the approach discussed in Sect. 3.3. In order to detect free surface

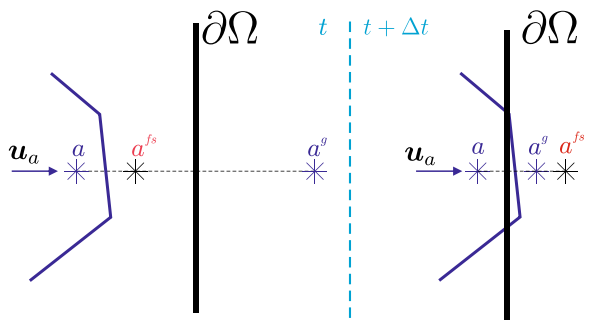

Fig. 6 Voronoi free-surface particle approaching a solid boundary

particles, the criterion discussed in Sect. 3.4.3 is evaluated for all particles within cell domains that contain at least one free-surface particle in the previous time step. In order to include the angle covered by the boundary, the reflected point a^g is included as part of the neighbors.

However, particles already on the free surface are free to collide with or get detached from a boundary. In this case no reflected point a^g is included in the free-surface criterion, leaving that region open to place a virtual free-surface particle a^{fs}. Then, the distance R_{a0}, defined in previous section, and the distance between the particle and its mirrored ghost particle are monitored (see left panel of Fig. 6). When the latter is smaller than the former (see right panel of Fig. 6), the particle is assumed to be in contact with the boundary and the solid boundary condition implementation discussed in Sect. 3.4.2 is applied. This approach provides a smooth transition between free surface and solid boundary conditions.

3.5 Shifting algorithms

As particles move, the resulting Voronoi cells tend to get distorted. Furthermore, a Voronoi diagram can have multiple generating particle configurations, which reflects the existence of glass modes that results in a progressive drift of the particles away from the center of mass of their cell. In order to balance these effects that reduce the precision of the differential operators, a shifting algorithm inspired by the Lloyd's method [14] can be used in the Voronoi sub-domain, similar to Springel [28]. When applied, the distance d_i between the particle and the cell center of mass $\boldsymbol{s}_a$ is monitorized, shifting the particle if exceeds certain given threshold according to Eq. (19).

$$\boldsymbol{r}_a^* = \boldsymbol{r}_a + \begin{cases} 0 & \text{for } \frac{d_i}{\eta\,\Delta x_a} < 0.9, \\ (\boldsymbol{s}_a - \boldsymbol{r}_a)\frac{d_i - 0.9\eta\,\Delta x_a}{0.2\eta\,\Delta x_a} & \text{for } 0.9 \le \frac{d_i}{\eta\,\Delta x_a} < 1.1, \\ \boldsymbol{s}_a - \boldsymbol{r}_a & \text{for } 1.1 \le \frac{d_i}{\eta\,\Delta x_a}, \end{cases} \tag{19}$$

where η is the coefficient that defines the reference threshold, typically set to $\eta = 0.25$.

4 Implementation

4.1 Code

The code key routines are written in C++, and the main time-stepping program is implemented in MATLAB. The code has been tested in 2D but is designed to work also in 3D. Parallelization has not been yet undertaken. The Voronoi tessellation requires 20% of the computation time. Apart from it, the performance of the code is similar to that of any standard serial SPH model.

4.2 Initialization

A physical domain, $\Omega_0 := \Omega(t = 0)$, and an initial density field, $\rho(\mathbf{x}, t = 0)$, are supposed to be known, together with a typical particle distance Δx. A Cartesian grid is built in Ω_0, keeping the minimum separation with the boundaries to be approximately $\Delta x/2$, and leading to a certain number of particles, N. A Voronoi tessellation is carried out rendering a vector of volumes, $\mathbf{V}$. The mass of each particle is then defined as $m_a = \rho(\mathbf{x}_a, 0)\ V_a$, and kept constant throughout the whole simulation.

From this Cartesian configuration, a stabilization scheme of the particle positions is executed, with the aim of finding an initial static condition. A linear damping term is added to the numerical model in order to accelerate the process of reaching a static equilibrium, as proposed by Monaghan [19]. For this reason, the momentum equation in (3) is modified to include the referred damping term, $-\xi\,\boldsymbol{u}_a$, while simultaneously removing the viscosity one:

$$\frac{\mathrm{d}\boldsymbol{u}_a}{\mathrm{d}t} = \boldsymbol{g}_a - \frac{1}{\rho_a}\sum_b (p_b + p_a)\,\nabla_a W_{ab}\,V_b - \xi\,\boldsymbol{u}_a, \tag{20}$$

where $\xi\,\Delta t = 0.05$.

During the stabilization phase, the maximum velocity and the total kinetic energy $\mathcal{E}_k$ are monitored. A characteristic time of the problem t_1 is defined. The stabilization evolves till $t/t_1 \sim 0.1$ and from then on, the stabilization continues until $\max_a |\mathbf{u}_a|/U < 0.01$, $\mathcal{E}_k^n/\mathcal{E}_0 < 0.001$, and $(\mathcal{E}_k^n - \mathcal{E}_k^{n-1})/\Delta t < 0.001\mathcal{E}_0/t_1$, with U being the characteristic velocity of the problem, $\mathcal{E}_0$ a reference energy, and n the time step index. Once this moment is reached, the particle setup is considered in equilibrium and the simulation can be launched. Some details of this phase are provided in some of the verification cases later in the paper.

In simulations with a free surface, the background pressure p_0 of the equation of state in (3) is set to zero, while in confined domain simulations, $p_0 := 0.05\,\rho\,c_0^2$.

4.3 Time-stepping

A leap frog predictor–corrector scheme is used in the simulations. The positions of the particles are advanced in time with an explicit second-order scheme, and both velocity (and density for the SPH particles) are predicted and afterward corrected [11,27]. The time step is affected by a CFL factor.

5 Verification

5.1 Hydrostatic equilibrium

This test case evaluates the ability of the presented numerical scheme to reach equilibrium from an unbalanced initial condition. The same configuration than the one studied by Colagrossi et al. [8] is analyzed here, consisting on a trapezoidal tank filled with fluid particles to a certain height and all initialized with atmospheric pressure. Under the presence of gravity, they should reach hydrostatic equilibrium if sufficient damping exists to attenuate the oscillations due to the elasticity of the fluid. The number of particles considered is 3125, and $\rho(\mathbf{x}, t = 0) = \rho_0$. Figure 7 shows the result obtained, with no noticeable difference in the pressure field between the Voronoi and SPH sub-domains indicating that the coupling is working adequately.

Figure 8 shows on the left panel the evolution of the kinetic energy of the system of particles. As can be appreciated, the inclusion of the linear damping terms quickly removes the acoustic-related oscillations present in the flow, bringing it rapidly to a static equilibrium. On the right panel, the pressure

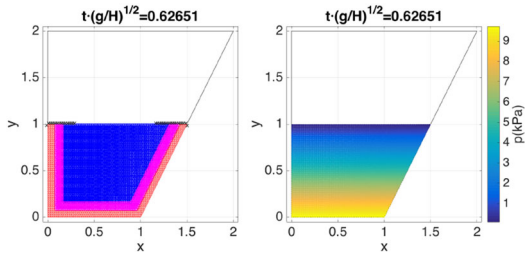

Fig. 7 Left: sub-domains in a hydrostatic equilibrium simulation (red VPH, magenta VPH-SPH coupling, blue SPH). Right: pressure field at the same time. (Colour figure online)

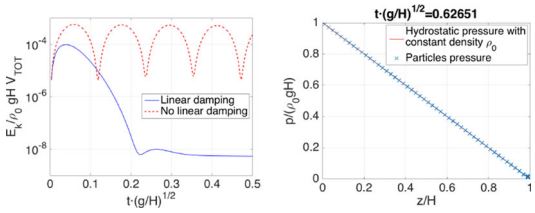

Fig. 8 Left: kinetic energy evolution with and without linear damping term; Right: particles's pressure distribution

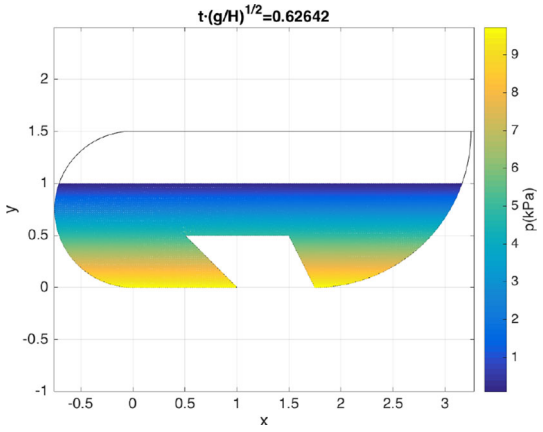

Fig. 9 Pressure field at hydrostatic equilibrium with a complex geometry from Colagrossi et al. [8]

is plotted as a function of the vertical position for all the particles in the fluid domain, showing reasonable agreement with the hydrostatic incompressible exact solution.

The second complex geometry presented by Colagrossi et al. [8] is also tested here, using 7400 particles in this case. Concave boundaries required special treatment since the Voronoi cells need to be trimmed. Figure 9 shows the results obtained, confirming the capability of the current numerical scheme to deal with more complex boundaries.

5.2 Sound wave

The propagation and ulterior reflection of a sound wave is discussed next, aiming at investigating how pressure-driven flows are treated by the coupled scheme. The case was first used by Ott and Schnetter [23] to assess the accuracy of a multiphase SPH implementation. In our case, a rectangular domain, periodic in y, is considered. The particles are evenly distributed and a small amplitude perturbation, $\Delta\rho(x)$, in their density is set according to the following formula:

$$\begin{aligned} \rho(x) &= \rho_0 + \Delta\rho(x) \\ &= \rho_0 + A\,\rho_0\,x^2\,\exp\left\{-\left(\frac{x - x_0}{W}\right)^2\right\}, \\ x &\in (0, 2) \end{aligned} \tag{21}$$

An initial horizontal velocity is given to the particles in order to privilege one propagation direction against the other,

$$u_x(x) = c_0 \frac{\Delta\rho(x)}{\rho_0}. \tag{22}$$

In addition, an artificial viscosity $\mu_{av} = 1/8\alpha\rho_0 h_0 c_0$ is included for numerical stability [15], where we take $\alpha = 0.02$ as widely used in SPH. 4k particles are used.

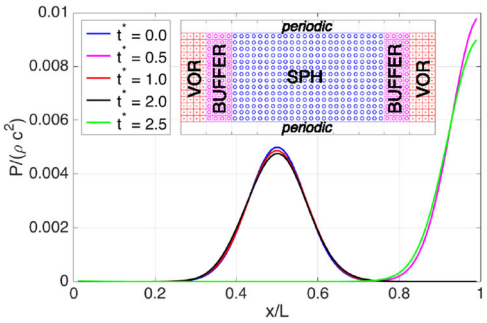

Fig. 10 2D sound wave propagation simulation. Pressure profiles

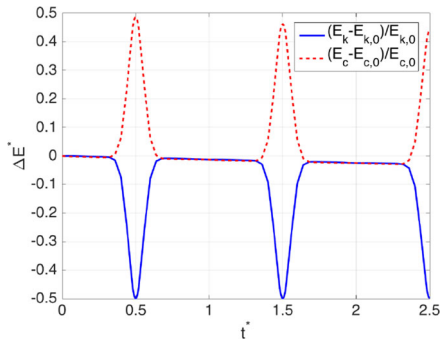

Fig. 11 Sound wave energy decay

A cross section of a 2D sound wave is shown as various time steps in Fig. 10, where $t^* = tc_s/L$. Since $x_0 = 0.5L$ is taken as the initial, position, $t^* = 1$ corresponds to the moment when the wave returns to the original position after one reflection. The results show how the wave maintains its shape reasonably well after its propagation, and reflection in the Voronoi region adjacent to the lateral walls.

Figure 11 shows the energy decay, taken as the difference with the initial value and made non-dimensional with the initial kinetic energy ($\Delta\mathcal{E}' = (\mathcal{E} - \mathcal{E}_0)/\mathcal{E}_0$). The figure shows the conversion between kinetic and elastic energy in the reflections, with an overall decay due to numerical dissipation. We can define the kinetic energy $\mathcal{E}_k$, and elastic energy $\mathcal{E}_c$ [3]:

$$\mathcal{E}_k = \sum_a 0.5 m_a \|\boldsymbol{v}_a\|^2, \tag{23}$$

$$\mathcal{E}_c = \sum_a \left[m_a c^2 \left(\log\left(\frac{\rho_a}{\rho_0}\right) + \frac{\rho_0}{\rho_a} - 1 \right) - m_a p_0 \frac{\rho_0 - \rho_a}{\rho_0 \rho_a} \right]. \tag{24}$$

5.3 2D Couette flow

A plane Couette flow starting from either the exact solution or starting from zero initial velocity is considered. 1 and 5.6 k particles have been used, respectively, and $\rho(\mathbf{x}, t = 0) = \rho_0$. Regarding the first case, from its analytical solution we can state that

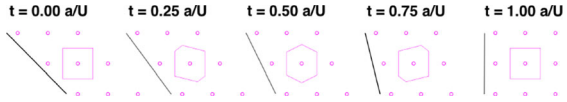

Fig. 12 Detail of one Voronoi cell at different time steps with the stationary Couette flow

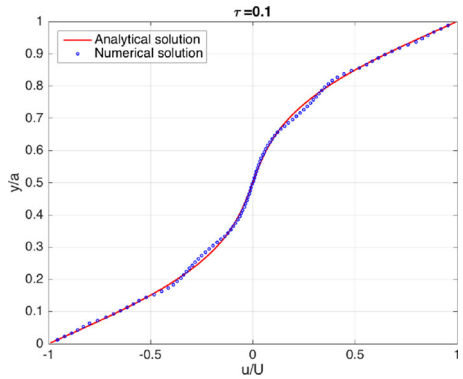

Fig. 13 Starting Couette velocity profile at $\tau = 0.1$ under $Re = 10$

$$\boldsymbol{v} = (Uy/a, 0) \rightarrow \boldsymbol{r}(t) = (x_0 + tUy/a, y_0),$$
$$\left.\begin{array}{l} \boldsymbol{r}_i(0) = (0,0), \\ \boldsymbol{r}_j(0) = (-z, z), z \in [0, a], \end{array}\right\} \rightarrow \left.\begin{array}{l} \boldsymbol{r}_i(a/U) = (0,0), \\ \boldsymbol{r}_j(a/U) = (0, z), \end{array}\right\},$$

where (x_0, y_0) represent the initial positions, U the upper wall velocity, and a the height of the channel. Therefore, all the particles located at a $-45°$ diagonal on the original Cartesian arrangement become vertically aligned after $t = a/U$, as can be observed in Fig. 12 where a detail of one Voronoi cell at different time steps is shown. The cells deform due to the different relative velocity recovering the original shape.

The starting Couette flow allows us to test the performance of the code under strong shear flows. The fluid is initialized at rest, with the upper boundary located at $y = a$ moving horizontally with velocity U in the positive x direction and the lower boundary at $y = 0$ moving with the same velocity but opposite direction, like the case presented by Monaghan [21]. Figure 13 shows the horizontal velocity profile along the vertical direction, under $Re = aU/\nu = 10$. The figure compares the numerical results with the theoretical solution given by Batchelor [6] and adapted to present boundary conditions,

$$\frac{u_x(t, y)}{U} = -\left(1 - \frac{2y}{a}\right) - \frac{2}{\pi} \sum_{j=1}^{\infty} \frac{1}{j} \sin(j\pi\tilde{y}) \exp(-j^2\pi^2\tau), \tag{25}$$

where $\tau = t\nu/\left[\rho_0 (a/2)^2\right]$ is a non-dimensional time based on the mean lifetime of the transition to stationary state, and $\tilde{y}$ indicates the distance to the closest boundary made

non-dimensional with $a/2$. The agreement is reasonable but small deviations from the exact solution are noticeable, which suggest that the approximation to the viscous term requires further assessment.

5.4 Lamb–Oseen vortex

This test case also represents a shear flow, in particular a pure viscous diffusion process. Its analytic solution is presented by Maciá et al. [15], where two types of fluid domains are considered for the numerical simulations: circular and square. The theoretical velocity and density distributions are assigned to the fluid particles as the initial conditions, leaving them free to move afterward under the sole no-slip boundary conditions on the enclosing walls.

$$\boldsymbol{v}(x, y, t) = (u, v) = q\frac{1 - \mathrm{e}^{-\frac{r^2}{a^2}}}{r^2}(-y, x), \tag{26}$$

$$a(t)^2 = a_0^2 + 4\nu t, \tag{27}$$

where q gives the intensity of the vortex, a is the effective vortex core radius where the velocity is maximum, ν is the kinematic viscosity, and $r = \|(x, y)\|$ is the magnitude of the position vector. Both circular and square configurations have been simulated using the same input values than Maciá et al.: $q = 0.5$, $a_0 = 1$, and $Re = \frac{2\pi q}{\nu} = 10$. Roughly 12 and 16 k particles have been used, respectively, and $\rho(\mathbf{x}, t = 0) = \rho_0$.

Figures 14 and 15 show the resulting velocity fields, displaying on their right the evolution of the calculated maximum velocity together with the analytic solution. The simulation results show a good agreement with the theoretical values.

Of particular relevance is the square domain case, since particles move across the buffer changing their weight values. However, the velocities in this zone are relatively small, making it difficult to extract conclusions.

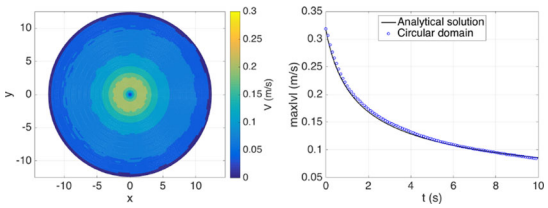

Fig. 14 Left: Lamb–Oseen vortex velocity fields in a circular domain at $t = 1$ s; Right: Evolution of max $\|\boldsymbol{v}\|$ of a Lamb–Ossen vortex

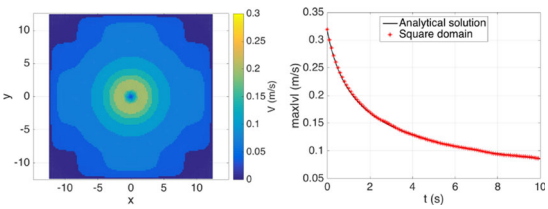

Fig. 15 Left: Lamb–Oseen vortex velocity fields in a square domain at $t = 1$ s; Right: Evolution of max $\|\boldsymbol{v}\|$ of a Lamb–Ossen vortex

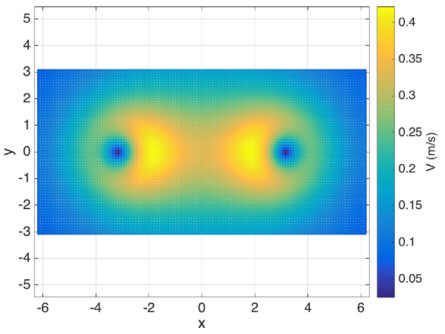

Fig. 16 Initial velocity field of two symmetric Lamb–Ossen vortices

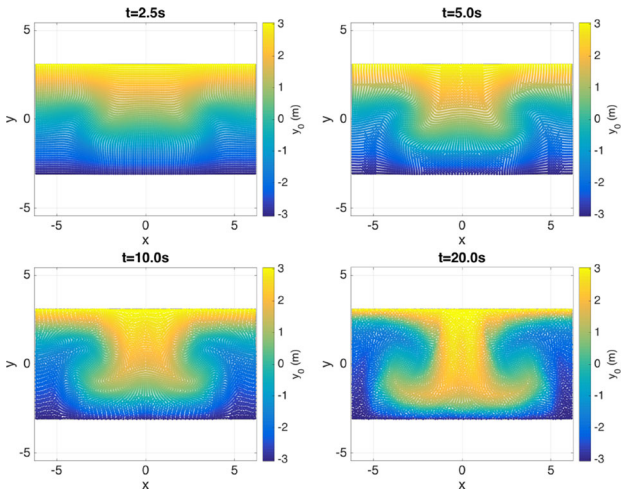

Fig. 17 Particle configuration at different time steps with the two symmetric Lamb–Ossen vortices

An alternative case with two symmetric Lamb–Ossen vortices has been simulated to visualize better this feature of the coupled scheme, as shown in Fig. 16. The same values of q, a_0, and ρ are used, although the walls are closer to the vortex centers in this case. The viscous dissipation is reduced by applying the free slip BC at the walls and reducing the viscosity to achieve $Re = \frac{2\pi q}{\nu} = 60$, which facilitates the movement of the particles.

Figure 17 shows the resulting particle distribution at various time steps. Each particle is colored based on its initial vertical position, $y_0 = y(t = 0)$. It can be observed how the mixing induced by the vortices leads to a movement of particles into and away from the walls, crossing smoothly the buffer zone. These results show how the coupled scheme is also able to transport mass across the buffer.

6 Conclusions

A hybrid Lagrangian Voronoi–SPH scheme, with an explicit weakly compressible formulation for both the Voronoi and

SPH sub-domains, has been developed. The SPH discretization is substituted by Voronoi elements close to solid boundaries. A buffer zone to couple the dynamics of both sub-domains is used. This zone is formed by a set of particles where fields are interpolated taking into account SPH particles and Voronoi elements. The accuracy of the coupled scheme is discussed by means of a set of well-known verification and validation benchmarks.

The results showed that pressure gradient dominated problems, such as hydrostatic conditions or sound wave propagations, are well simulated by the method. However, problems which are dominated by viscous diffusion render less accurate results, suggesting that the approximation to the second-order derivatives requires further assessment and likely improvement.

Acknowledgements The authors thank Francisco J. Dominguez for assistance with the artwork. Antonio Souto-Iglesias acknowledges the support of Universidad Politécnica de Madrid for funding his leave in UC Berkeley Department of Mechanical Engineering from September 2016 until June 2017.

Compliance with ethical standard

Conflicts of interest On behalf of all authors, the corresponding author states that there is no conflict of interest.

References

1. Antuono M, Colagrossi A, Marrone S, Molteni D (2010) Free-surface flows solved by means of SPH schemes with numerical diffusive terms. Comput Phys Commun 181(3):532–549. https://doi.org/10.1016/j.cpc.2009.11.002
2. Antuono M, Colagrossi A, Marrone S (2012) Numerical diffusive terms in weakly-compressible SPH schemes. Comput Phys Commun 183(12):2570–2580. https://doi.org/10.1016/j.cpc.2012.07.006
3. Antuono M, Marrone S, Colagrossi A, Bouscasse B (2015) Energy balance in the δ-SPH scheme. Comput Methods Appl Mech Eng 289:209–226
4. Barcarolo DA (2013) Improvement of the precision and the efficiency of the SPH method: theoretical and numerical study. Ph.D. thesis, Ecole Centrale de Nantes
5. Barcarolo DA, Touzé DL, Oger G, de Vuyst F (2014) Voronoi-SPH: on the analysis of a hybrid finite volumes-smoothed particle hydrodynamics method. In: 9th international SPHERIC workshop, pp 371–378
6. Batchelor GK (1967) Introduction to fluid dynamics. Cambridge University Press, New York
7. Cercos-Pita J (2015) AQUAgpusph, a new free 3D SPH solver accelerated with OpenCL. Comput Phys Commun 192:295–312. https://doi.org/10.1016/j.cpc.2015.01.026
8. Colagrossi A, Bouscasse B, Antuono M, Marrone S (2012) Particle packing algorithm for SPH schemes. Comput Phys Commun 183(2):1641–1683
9. Colagrossi A, Souto-Iglesias A, Antuono M, Marrone S (2013) Smoothed-particle-hydrodynamics modeling of dissipation mechanisms in gravity waves. Phys Rev E 87(023):302
10. Duque D, Español P, de la Torre JA (2017) Extending linear finite elements to quadratic precision on arbitrary meshes. Appl Math Comput 301:201–213. https://doi.org/10.1016/j.amc.2016.12.010
11. Gray J (2001) Caldera collapse and the generation of waves. Ph.D. thesis, Monash University
12. Hess S, Springel V (2010) Particle hydrodynamics with tessellation techniques. Mon Not R Astron Soc 406(4):2289–2311. https://doi.org/10.1111/j.1365-2966.2010.16892.x
13. Kumar P, Yang Q, Jones V, McCue-Weil L (2015) Coupled SPH-FVM simulation within the OpenFOAM framework. Procedia IUTAM 18:76–84. https://doi.org/10.1016/j.piutam.2015.11.008
14. Lloyd S (1982) Least squares quantization in PCM. IEEE Trans Inf Theory 28(2):129–137. https://doi.org/10.1109/TIT.1982.1056489
15. Macià F, Sánchez JM, Souto-Iglesias A, González LM (2012) WCSPH viscosity diffusion processes in vortex flows. Int J Numer Methods Fluids 69(3):509–533
16. Marrone S, Antuono M, Colagrossi A, Colicchio G, Le Touzé D, Graziani G (2011) Delta-SPH model for simulating violent impact flows. Comput Methods Appl Mech Eng 200(13–16):1526–1542. https://doi.org/10.1016/j.cma.2010.12.016
17. Marrone S, Colagrossi A, Antuono M, Colicchio G, Graziani G (2013) An accurate SPH modeling of viscous flows around bodies at low and moderate Reynolds numbers. J Comput Phys 245:456–475. https://doi.org/10.1016/j.jcp.2013.03.011
18. Marrone S, Mascio AD, Le Touzé D (2016) Coupling of smoothed particle hydrodynamics with finite volume method for free-surface flows. J Comput Phys 310:161–180 available online 11 December 2015
19. Monaghan J (1994) Simulating free surface flows with SPH. J Comput Phys 110(2):39–406
20. Monaghan J (2012) Smoothed particle hydrodynamics and its diverse applications. Ann Rev Fluid Mech 44(1):323–346
21. Monaghan JJ (2005) Smoothed particle hydrodynamic simulations of shear flow. Mon Not R Astron Soc 365:199–213. https://doi.org/10.1111/j.1365-2966.2005.09783.x
22. Napoli E, Marchis MD, Gianguzzi C, Milici B, Monteleone A (2016) A coupled finite volume-smoothed particle hydrodynamics method for incompressible flows. Comput Methods Appl Mech Eng 310:674–693. https://doi.org/10.1016/j.cma.2016.07.034
23. Ott F, Schnetter E (2003) A modified SPH approach for fluids with large density differences. arXiv:physics/0303112
24. Quinlan NJ, Lastiwka M, Basa M (2006) Truncation error in mesh-free particle methods. Int J Numer Methods Eng 66(13):2064–2085. https://doi.org/10.1002/nme.1617
25. Serrano M (2006) Comparison between smoothed dissipative particle dynamics and Voronoi fluid particle model in a shear stationary flow. Phys A Stat Mech Appl 362(1):204–209. https://doi.org/10.1016/j.physa.2005.09.024
26. Serrano M, Español P (2001) Thermodynamically consistent mesoscopic fluid particle model. Phys Rev E 64(046):115. https://doi.org/10.1103/PhysRevE.64.046115
27. Souto-Iglesias A, Delorme L, Pérez-Rojas L, Abril-Pérez S (2006) Liquid moment amplitude assessment in sloshing type problems with smooth particle hydrodynamics. Ocean Eng 33(11–12):1462–1484
28. Springel V (2010) E pur si muove: Galilean-invariant cosmological hydrodynamical simulations on a moving mesh. Monthly Notices of the Royal Astronomical Society 401(2):791. https://doi.org/10.1111/j.1365-2966.2009.15715.x